Science Advances
AAAS

advances.sciencemag.org/cgi/content/full/6/41/eabb0694/DC1

Supplementary Materials for

Designing hierarchical nanoporous membranes for highly efficient gas adsorption and storage

Haiyan Mao, Jing Tang, Jun Chen, Jiayu Wan, Kaipeng Hou, Yucan Peng, David M. Halat, Liangang Xiao, Rufan Zhang, Xudong Lv, Ankun Yang, Yi Cui*, Jeffrey A. Reimer*

*Corresponding author. Email: yicui@stanford.edu (Y.C.); reimer@berkeley.edu (J.A.R.)

Published 7 October 2020, *Sci. Adv.* **6**, eabb0694 (2020)
DOI: 10.1126/sciadv.abb0694

This PDF file includes:

Sections S1 to S4
Figs. S1 to S5
Tables S1 to S3
References

Effect of the reaction temperature on the morphology of carbon spheres

Figure S1 shows the microscopic morphology of the cellulose hydrothermal carbonization product at a cellulose concentration of 0.04 g ml^{-1} after 5 h at different reaction temperatures. **Figure 2C** shows the microscopic morphology of uncarbonized cellulose, and with a hydrothermal temperature of 200 °C (**Fig. S1A**), the morphology of the carbon spheres clearly remains nanofibrous. However, small carbon spheres already appear on the surface of the fiber, indicating that cellulose begins to undergo carbonization into spheres at 200 °C. When the temperature increases to 220 °C, the extent of the reaction is still relatively small (**Fig. S1B**). **Figure S1B** shows that with the increased hydrothermal reaction temperature, most of the original fibrous morphology disappears. However, the carbon spheres clearly show evidence of fusion phenomena. Most of the reaction products do not form a complete spherical morphology, and the carbon spheres are unevenly distributed. The particle sizes of the carbon spheres are distributed over a wide range, with both μm-sized and nm-sized spheres. **Figure 2, (D and E)** reveals that when the hydrothermal temperature reaches 240 °C, the fusion phenomena do not occur, and the hydrothermal products have a high degree of sphericity, uniform distribution, narrow distribution of particle size, and an average diameter of 2-3 μm. The surfaces of the carbon spheres are smooth and separated from each other. **Figure S1C** shows the aggregation phenomenon among carbon spheres when the temperature increases to 260 °C.

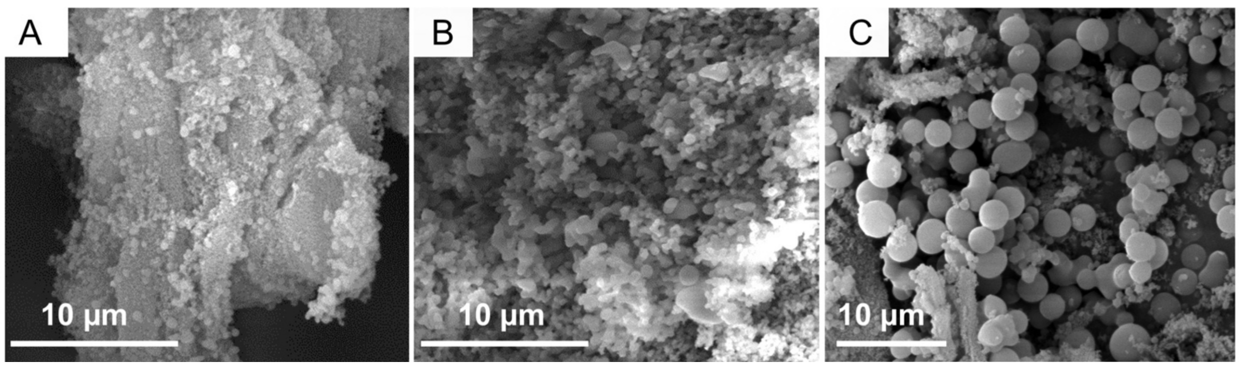

Figure S1 | SEM micrographs of cellulose and carbon spheres at various temperatures. SEM of carbon spheres obtained by hydrothermal treatment of cellulose at 200 °C (A), 220 °C (B), and 260 °C (C).

Effect of the reaction time on the morphology of the carbon spheres

Figure S2 shows the change in the SEM micrographs when the carbonization time was extended from 3 h to 7 h at a carbonization temperature of 240 °C and a cellulose reaction concentration of 0.04 g ml^{-1}. As shown in **Figure S2A**, when the carbonization time is 3 h, very few carbon spheres reach a particle size of 2 μm, and the majority of the carbon spheres are amorphous. As the carbonization time increases to 5 h, the particle size of the carbon spheres increases from 1.5 μm in **Fig. S2A** to 2 μm in **Fig. 2E**. When the time is further increased to 7 h, the particle size of the carbon spheres increases from 2.0 μm (in **Fig. 2E**) to 2.5 μm (in **Fig. S2B**). The longer reaction time is responsible for the larger particle size of the carbon spheres. However, an aggregation phenomenon occurs to some extent, and the high temperature is related to the severity of aggregation. The formation of aggregates of deformed carbon spheres may be attributed to the fact that mechanical stirring does not ensure complete uniformity of cellulose in the system. With the high concentrations of carbon spheres, aggregation is prone to occur when the carbon spheres increase in size, leading to deformed carbon spheres. With a reaction time of 7 h, cellulose is deposited at the bottom of the reaction vessel, resulting in a relatively large concentration of carbon spheres at the bottom. It can be concluded that the optimal hydrothermal reaction temperature and time for preparing cellulose-based carbon spheres are 240 °C and 5 h, respectively.

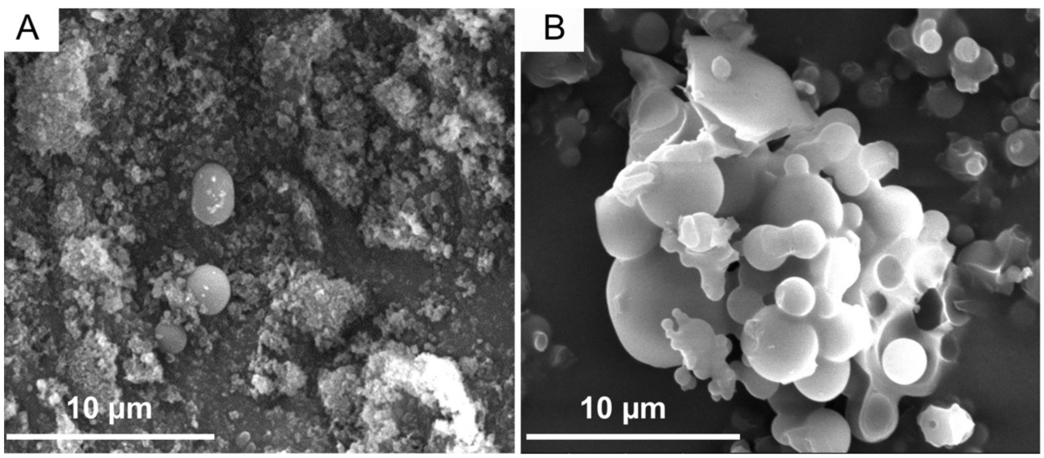

Figure S2 | SEM micrographs of carbon spheres obtained by hydrothermal treatment of cellulose at various times: 3 h (A) and 7 h (B) (the carbonization temperature and concentration were 240 °C and 0.04 g ml^{-1}, respectively).

Effect of the reaction concentration on the morphology of carbon spheres

Figure S3 shows the microscopic morphology of cellulose products at different concentrations undergoing hydrothermal carbonization for 5 h at 240 °C. When the cellulose concentration is increased from 0.02 g ml^{-1} to 0.03 g ml^{-1}, the diameter of the carbon spheres increases to 2 μm (**Fig. S3B**), but the diameter decreases to 1.5 μm at 0.04 g ml^{-1} (**Fig. 2E**). When the concentration increases from 0.04 g ml^{-1} (**Fig. 2E**) to 0.05 g ml^{-1} (**Fig. S3C**), the diameter of some carbon spheres increases, but the diameter of a few individual carbon spheres continues to decrease. Aggregation of carbon spheres also occurs. It is clear that although the particle size of the resulting carbon spheres reaches a maximum at a cellulose concentration of 0.05 g ml^{-1}, the sphericity of the carbon spheres is not uniform, and aggregation occurs. Therefore, the optimal cellulose concentration for the preparation of cellulose-based carbon spheres is 0.04 g ml^{-1}.

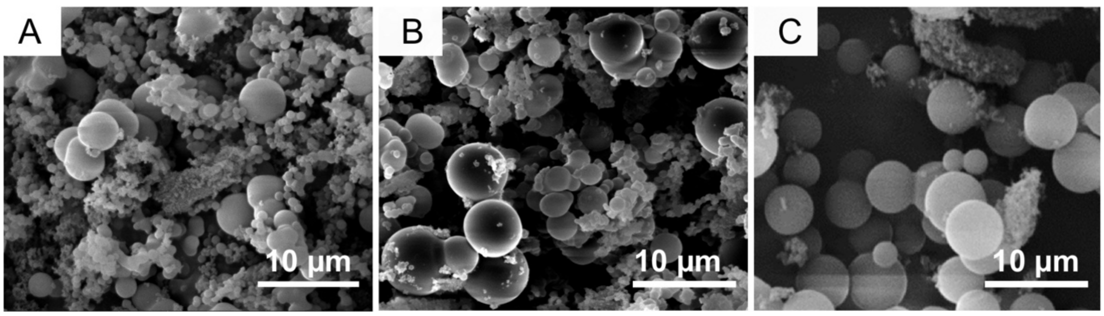

Figure S3 | SEM micrographs of carbon spheres obtained by hydrothermal treatment of cellulose at various concentrations: 0.02 g ml^{-1} (A), 0.03 g ml^{-1} (B), and 0.05 g ml^{-1} (C); the carbonization temperature and time were 240 °C and 5 h, respectively.

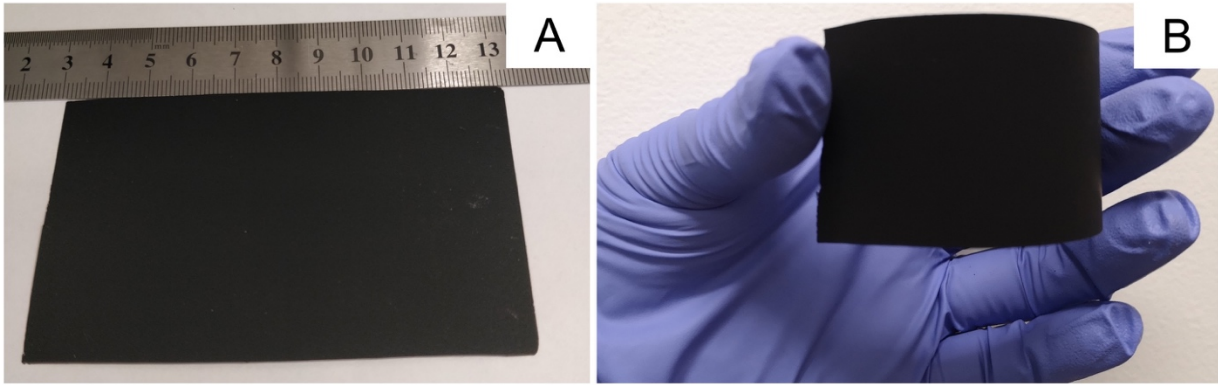

Figure S4 | Photographs of the hierarchical nanoporous membranes created using a doctor blade coating method. **A,** Photograph of large-area HNM (10 × 10 cm^2) fabricated by a doctor-blade method. **B,** Photograph of free-standing and flexible HNM without absence of cracks. Photo credit: J.T., Stanford University. Permission granted.

Table S1. Surface area, micropore surface area, micropore volume, and total pore volume of carbon spheres and HCS formed at a carbonization temperature of 240 °C, carbonization time of 5 h, and cellulose concentration of 0.04 g/ml.

	Surface area (m^2/g)	**Micropore surface area (m^2/g)**	**Micropore volume (cc/g)**	**Mesopore volume (cc/g)**	**Total pore volume (cc/g)**
Carbon sphere	528	50	0.016	0.046	0.098
HCS	2551	1957	0.796	0.120	0.916

Dubinin-Radushkevich fitting of VOC adsorption isotherms

In the actual adsorption process, the adsorption is not at equilibrium, and both adsorption and desorption processes occur at the same time. In order to investigate the mechanism of adsorption equilibrium for toluene/acetone, the Dubinin-Radushkevich model (*36*) was employed to fit the adsorption isotherm experimental data. Major parameters that may affect the adsorption process include the surface performance of the GO/HCS composite membranes, concentration of toluene/acetone, and temperature.

The Dubinin-Radushkevich (DR) equation is expressed as (*36*):

$$q = W_0 \exp\left[-\left(\frac{(RT\ln(p_0/p)}{E}\right)^2\right]$$ **Equation S1**

Where q is the adsorption capacity (%, mass) of the adsorbate, p/p_0 is the relative pressure (the ratio of adsorbate vapor pressure to saturated vapor pressure), and E and W_0 are constants that depend only on the adsorbate properties of the pore volume and surface area. In this study, k and W_0 can be calculated from the adsorption isotherm data.

Table S2. Dubinin-Radushkevich model fit parameters for toluene and acetone adsorption on HNM.

Adsorbate	*E* (kJ/mol)	W_0 (cc/g)	Mean relative error (%)	R^2	ΔH (kJ/mol)
Acetone	24.5	0.754	6.5	0.936	24
Toluene	48.2	0.792	3.5	0.985	49

Table S3. VOC adsorption capacity and yields of HNM regenerated over five cycles.

Cycles	Adsorption capacity (mg/g)		Yield (%)	
	Toluene	Acetone	Toluene	Acetone
0	372.0	248.3	-	-
1	369.1	245.1	99.8	99.4
2	371.5	246.6	99.5	98.9
3	366.2	247.3	98.4	98.8
4	369.3	244.1	98.3	98.5
5	366.5	246.0	98.3	98.4

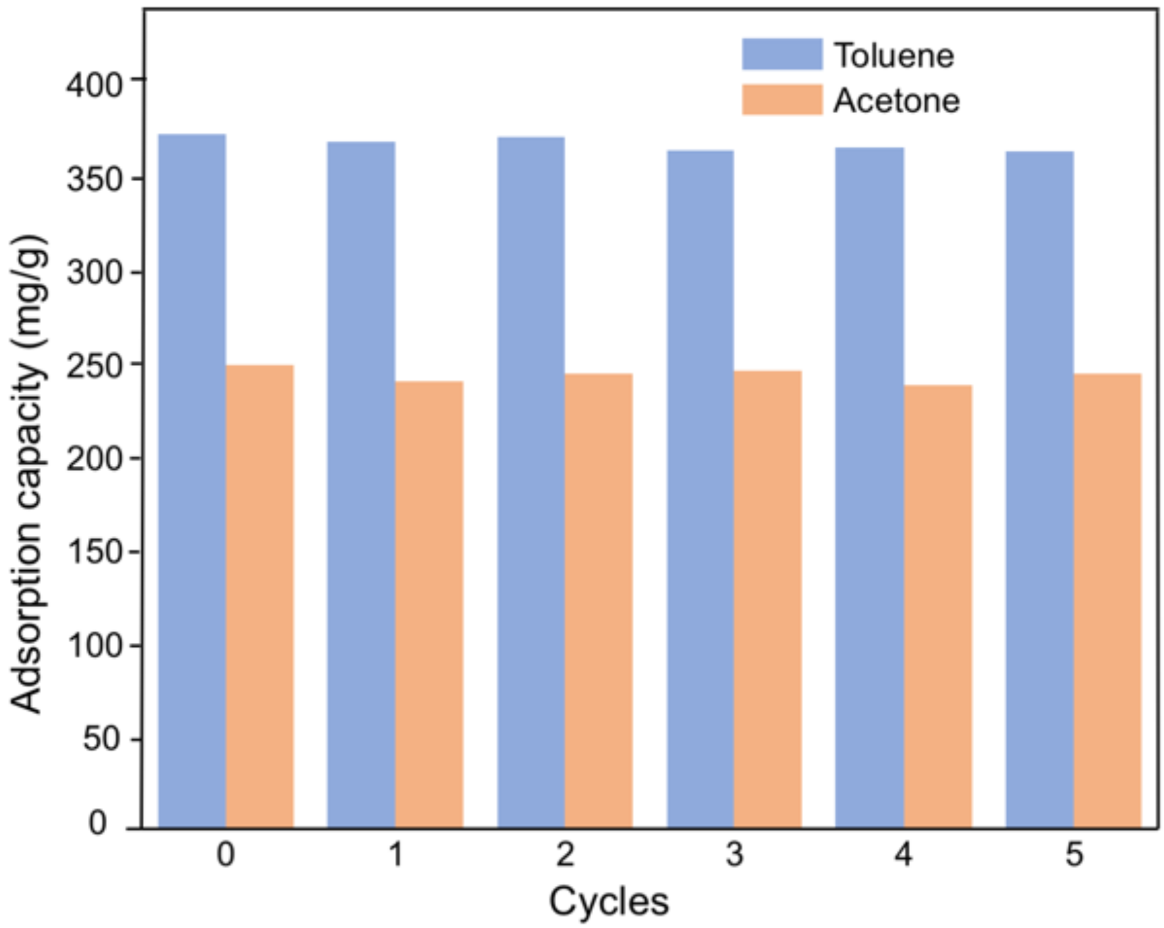

Figure S5 | VOC adsorption-desorption onto HNM over five cycles.

REFERENCES AND NOTES

1. W. Liu, S.-D. Jiang, Y. Yan, W. Wang, J. Li, K. Leng, S. Japip, J. Liu, H. Xu, Y. Liu, I.-H. Park, Y. Bao, W. Yu, M. D. Guiver, S. Zhang, K. P. Loh, A solution-processable and ultra-permeable conjugated microporous thermoset for selective hydrogen separation. *Nat. Commun.* **11**, 1633 (2020).

2. J. Liu, N. P. Wickramaratne, S. Z. Qiao, M. Jaroniec, Molecular-based design and emerging applications of nanoporous carbon spheres. *Nat. Mater.* **14**, 763–774 (2015).

3. X. Xie, C. Chen, N. Zhang, Z.-R. Tang, J. Jiang, Y.-J. Xu, Microstructure and surface control of MXene films for water purification. *Nat. Sustain.* **2**, 856–862 (2019).

4. S. Yi, B. Ghanem, Y. Liu, I. Pinnau, W. J. Koros, Ultraselective glassy polymer membranes with unprecedented performance for energy-efficient sour gas separation. *Sci. Adv.* **5**, eaaw5459 (2019).

5. P. Li, J. Li, X. Feng, J. Li, Y. Hao, J. Zhang, H. Wang, A. Yin, J. Zhou, X. Ma, B. Wang, Metal-organic frameworks with photocatalytic bactericidal activity for integrated air cleaning. *Nat. Commun.* **10**, 2177 (2019).

6. J. E. Bachman, Z. P. Smith, T. Li, T. Xu, J. R. Long, Enhanced ethylene separation and plasticization resistance in polymer membranes incorporating metal–organic framework nanocrystals. *Nat. Mater.* **15**, 845–849 (2016).

7. M. Y. Jeon, D. Kim, P. Kumar, P. S. Lee, N. Rangnekar, P. Bai, M. Shete, B. Elyassi, H. S. Lee, K. Narasimharao, S. N. Basahel, S. Al-Thabaiti, W. Xu, H. J. Cho, E. O. Fetisov, R. Thyagarajan, R. F. Dejaco, W. Fan, K. A. Mkhoyan, J. I. Siepmann, M. Tsapatsis, Ultra-selective high-flux membranes from directly synthesized zeolite nanosheets. *Nature* **543**, 690–694 (2017).

8. L.-H. Xie, X.-M. Liu, T. He, J.-R. Li, Metal-organic frameworks for the capture of trace aromatic volatile organic compounds. *Chem* **4**, 1911–1927 (2018).

9. E. Y. Lee, M. P. Suh, A robust porous material constructed of linear coordination polymer chains: Reversible single-crystal to single-crystal transformations upon dehydration and rehydration. *Angew. Chem. Int. Ed.* **43**, 2798–2801 (2004).

10. J. Abraham, K. S. Vasu, C. D. Williams, K. Gopinadhan, Y. Su, C. T. Cherian, J. Dix, E. Prestat, S. J. Haigh, I. V. Grigorieva, P. Carbone, A. K. Geim, R. R. Nair, Tunable sieving of ions using graphene oxide membranes. *Nat. Nanotechnol.* **12**, 546–550 (2017).

11. J. Zhao, G. Zhou, K. Yan, J. Xie, Y. Li, L. Liao, Y. Jin, K. Liu, P.-C. Hsu, J. Wang, H.-M. Cheng, Y. Cui, Air-stable and freestanding lithium alloy/graphene foil as an alternative to lithium metal anodes. *Nat. Nanotechnol.* **12**, 993–999 (2017).

12. S. Wang, D. Mahalingam, B. Sutisna, S. P. Nunes, 2D-dual-spacing channel membranes for high performance organic solvent nanofiltration. *J. Mater. Chem. A* **7**, 11673–11682 (2019).

13. B. Lu, X. Yuan, Y. Ren, Q. Shi, S. Wang, J. Dong, Z.-d. Nan, Cost-effective three dimensional Ag/polymer dyes/graphene-carbon spheres hybrids for high performance nonenzymatic sensor and its application in living cell H_2O_2 detection. *Bioelectrochemistry* **123**, 103–111 (2018).

14. X. Zheng, G. Shen, C. Wang, Y. Li, D. Dunphy, T. Hasan, C. J. Brinker, B.-L. Su, Bio-inspired Murray materials for mass transfer and activity. *Nat. Commun.* **8**, 14921 (2017).

15. C. Falco, N. Baccile, M.-M. Titirici, Morphological and structural differences between glucose, cellulose and lignocellulosic biomass derived hydrothermal carbons. *Green Chem.* **13**, 3273–3281 (2011).

16. R. Li, A. Shahbazi, A review of hydrothermal carbonization of carbohydrates for carbon spheres preparation. *Trends Renew. Energ.* **1**, 43–56 (2015).

17. Y. Mi, W. Hu, Y. Dan, Y. Liu, Synthesis of carbon micro-spheres by a glucose hydrothermal method. *Mater. Lett.* **62**, 1194–1196 (2008).

18. T. Li, S. X. Li, W. Kong, C. Chen, E. Hitz, C. Jia, J. Dai, X. Zhang, R. Briber, Z. Siwy, M. Reed, L. Hu, A nanofluidic ion regulation membrane with aligned cellulose nanofibers. *Sci. Adv.* **5**, eaau4238 (2019).

19. M. Sevilla, A. B. Fuertes, The production of carbon materials by hydrothermal carbonization of cellulose. *Carbon* **47**, 2281–2289 (2009).

20. S. Brunauer, L.S. Deming,W.E. Deming, and E. Teller, On a theory of the van der waals adsorption of gases. J. Am. Chem. Soc. 62, 1723–1732 (1940).

21. L. Jiang, L. Sheng, C. Long, Z. Fan, Densely packed graphene nanomesh-carbon nanotube hybrid film for ultra-high volumetric performance supercapacitors. *Nano Energy* **11**, 471–480 (2015).

22. S. Brunauer, P. H. Emmett, E. Teller, Adsorption of gases in multimolecular layers. *J. Am. Chem. Soc.* **60**, 309–319 (1938).

23. N. Zhang, N. Gao, C. Fu, D. Liu, S. Li, L. Jiang, H. Zhou, Y. Kuang, Hierarchical porous carbon spheres/graphene composite for supercapacitor with both aqueous solution and ionic liquid. *Electrochim. Acta* **235**, 340–347 (2017).

24. H. Li, K. Wu, J. Lim, H.-J. Song, V. I. Klimov, Doctor-blade deposition of quantum dots onto standard window glass for low-loss large-area luminescent solar concentrators. *Nat. Energy* **1**, 16157 (2016).

25. K. Vellingiri, P. Kumar, A. Deep, K.-H. Kim, Metal-organic frameworks for the adsorption of gaseous toluene under ambient temperature and pressure. *Chem. Eng. J.* **307**, 1116–1126 (2017).

26. H. Irvani, M. Pour, A. Vahidi, S. Arezoomandan, H. S.-F. Abady, Removal of toluene vapors from the polluted air with modified natural zeolite and titanium dioxide nanoparticles. *Med. Gas Res.* **8**, 91–97 (2018).

27. M. A. Lillo-Ródenas, D. Cazorla-Amorós, A. Linares-Solano, Behaviour of activated carbons with different pore size distributions and surface oxygen groups for benzene and toluene adsorption at low concentrations. *Carbon* **43**, 1758–1767 (2005).

28. H. Wang, S. Min, C. Ma, Z. Liu, W. Zhang, Q. Wang, D. Li, Y. Li, S. Turner, Y. Han, H. Zhu, E. Abou-Hamad, M. N. Hedhili, J. Pan, W. Yu, K.-W. Huang, L.-J. Li, J. Yuan, M. Antonietti, T. Wu, Synthesis of single-crystal-like nanoporous carbon membranes and their application in overall water splitting. *Nat. Commun.* **8**, 13592 (2017).

29. F. Xu, Z. Tang, S. Huang, L. Chen, Y. Liang, W. Mai, H. Zhong, R. Fu, D. Wu, Facile synthesis of ultrahigh-surface-area hollow carbon nanospheres for enhanced adsorption and energy storage. *Nat. Commun.* **6**, 7221 (2015).

30. C. Buttersack, Modeling of type IV and V sigmoidal adsorption isotherms. *Phys. Chem. Chem. Phys.* **21**, 5614–5626 (2019).

31. R. Li, S. Chong, N. Altaf, Y. Gao, B. Louis, Q. Wang, Synthesis of ZSM-5/siliceous zeolite composites for improvement of hydrophobic adsorption of volatile organic compounds. *Front. Chem.* **7**, 505 (2019).

32. M. Baca, K. Cendrowski, P. Banach, B. Michalkiewicz, E. Mijowska, R. J. Kalenczuk, Effect of Pd loading on hydrogen storage properties of disordered mesoporous hollow carbon spheres. *Int. J. Hydrogen Energy* **42**, 30461–30469 (2017).

33. D. J. Levine, T. Runčevski, M. T. Kapelewski, B. K. Keitz, J. Oktawiec, D. A. Reed, J. A. Mason, H. Z. H. Jiang, K. A. Colwell, C. M. Legendre, S. A. Fitzgerald, J. R. Long, Olsalazine-based metal-organic frameworks as biocompatible platforms for H_2 adsorption and drug delivery. *J. Am. Chem. Soc.* **138**, 10143–10150 (2016).

34. V. Abdelsayed, S. Moussa, H. M. Hassan, H. S. Aluri, M. M. Collinson, M. S. El-Shall, Photothermal deoxygenation of graphite oxide with laser excitation in solution and graphene-aided increase in water temperature. *J. Phys. Chem. Lett.* **1**, 2804–2809 (2010).

35. T. Munakata, Density functional theory and langevin-diffusion equation. *Strongly Coupled Plasma Phys.* **1990**, 695–698 (1990).

36. I. I. Laskar, Z. Hashisho, Insights into modeling adsorption equilibria of single and multicomponent systems of organic and water vapors. *Sep. Purif. Technol.* 241, 116681 (2020).